



1                   **Asian Summer Monsoon Anticyclone: Trends and Variability**

2                   Ghouse Basha<sup>1</sup>, M. Venkat Ratnam<sup>1</sup> and Pangaluru Kishore<sup>2</sup>  
3                   <sup>1</sup>National Atmospheric Research Laboratory, Department of Space, Gadanki-517112, India.

4                   <sup>2</sup> Department of Earth System Science, University of California, Irvine, CA, 92697, USA.

5                   Correspondence to: Ghouse Basha (mdbasha@narl.gov.in)

6                   **Abstract**

7                   The Asian Summer Monsoon (ASM) dynamics act as a pathway for the transport of  
8 trace gases and pollutants both vertically (through convection) and horizontally (through low-  
9 level jet and tropical easterly jet). These pollutants will be trapped in the anticyclone present  
10 during the same period in the upper troposphere and lower stratosphere (UTLS). Since the  
11 anticyclone extends from the Middle East to East Asia, trapped pollutants are expected to  
12 make a large radiative forcing to the background atmosphere. Thus, it is essential to  
13 understand the anticyclone features in detail and its relation to long-term oscillations. This  
14 work explores the spatial variability and the trends of the Asian Summer Monsoon  
15 Anticyclone (ASMA) using observational and reanalysis data sets. Emphasis is made to  
16 investigate the temporal, spatial, and long-term trends of ASMA. Our analysis indicates that  
17 the spatial extent and magnitude of ASMA is greater during July and August compared to  
18 June and September. The decadal variability of the anticyclone is very large at the edges of  
19 anticyclone than at the core region. Significant deviations in the northeast and southwest parts  
20 of ASMA are also observed in the decadal variability with reference to 1951-1960 period.  
21 The strength of the ASMA shows a drastic increase from the easterlies to the westerlies in  
22 terms of temporal variation. Further, our results show that the extent of anticyclone is greater  
23 during the active phase of the monsoon, strong monsoon years, and during La Niña events.  
24 Significant warming with strong westerlies is observed exactly over the Tibetan Plateau  
25 during the active phase of the monsoon, strong monsoon years, and during La Niña events.  
26 Over the Tibetan Plateau, there is strong elevated heating from the surface to the tropopause,



27 which is observed with strong westerlies during active and strong monsoon years. Our results  
28 support the transport process over Tibetan Plateau and the Indian region during active, strong  
29 monsoon years and during strong La Niña years. It is suggested to consider different phases  
30 of monsoon while interpreting the pollutants/trace gases in the anticyclone.

31 *Keywords:* Asian Monsoon, anticyclone, geopotential height, La Niño, El Niño, and rainfall

## 32 **1. Introduction**

33 The Asian Summer Monsoon Anticyclone (ASMA) is a dominant circulation in the  
34 Northern Hemisphere (NH) summer in the Upper Troposphere and Lower Stratosphere  
35 (UTLS), which extends from Asia to the Middle East. ASMA is bordered by the subtropical  
36 westerly jet in the north and easterly jets to the south. ASMA circulation responds to heating  
37 corresponding to the deep convection of the south Asian monsoon (Hoskins and Rodwell,  
38 1995; Highwood and Hoskins, 1998). This strong anticyclone circulation isolates the air and  
39 is tied to the outflow of deep convection, which has distant maxima characters in terms of  
40 dynamical variability and chemical characteristics (Randel and Park, 2006; Park et al., 2007).  
41 The maximum occurs due to strong winds and closed streamlines of an anticyclone, which  
42 isolate the air within the anticyclone and it is very dynamic in nature (e.g. Vogel et al., 2016).

43 Recently, the anticyclone circulation in UTLS has been paid more attention by  
44 researchers in order to understand dynamics, chemistry and radiation of the region. The  
45 dynamical confinement of tropospheric tracers and aerosols in the anticyclone isolate them  
46 from the surrounding air displaying distinct maxima near the tropopause. This issue has been  
47 discussed by several authors (e.g., Park et al., 2007; Fadnavis et al., 2014; Glatthor et al.,  
48 2015; Vernier et al., 2015; Santee et al., 2017). Deep convection during monsoon can  
49 transport tropospheric tracers from the surface to the UTLS (Vogel et al., 2015; Tissier and  
50 Legras, 2016). The confined tracers transported outside the edge of the anticyclone will affect  
51 the trace gas concentration in the UTLS resulting in significant changes in radiative forcings



52 (Solomon et al., 2010; Riese et al., 2012; Hossaini et al., 2015). The centre of the anticyclone  
53 is located either over the Iranian Plateau or over the Tibetan Plateaus where the distribution  
54 of pollutants and tracers vary significantly (Yan et al., 2011).

55 The spatial extent, strength, and the location of an anticyclone vary on several  
56 temporal scales caused by internal dynamical variability of the Asian monsoon (Zhang et al.,  
57 2002; Randel and Park, 2006; Garny and Randel, 2013; Vogel et al., 2015; Pan et al., 2016).  
58 However, the variability of anticyclone structure and response to Indian monsoon are not  
59 understood. Therefore, in the first part of the study, we investigate the spatial, inter-annual  
60 and decadal variations of the anticyclone. Since the Indian monsoon responds in different  
61 time scales, we also investigated the anticyclone variability with respect to the wet and dry  
62 spells of the Indian monsoon, strong and weak monsoon years, and the stronger El Nino  
63 Southern Oscillation (ENSO) years. For this, we have utilized the NCEP/NCAR reanalysis  
64 geopotential height from 1948 to 2016. The structure of the paper is as follows. We describe  
65 the data sets used in this study in Section 2. Section 3 contains the seasonal and decadal  
66 variation of the anticyclone and its relation with large scale oscillations. Section 4 shows the  
67 influence of days with wet and dry spells, strong and weak monsoon years, and ENSO's  
68 effects on the anticyclone. Finally, we discuss our results in Section 5.

## 69 **2. Data and Methodology**

### 70 **2.1. NCEP/NCAR Reanalysis**

71 The National Centers for Environmental Prediction (NCEP), in collaboration with the  
72 National Center for Atmospheric Research (NCAR) produces reanalysis data from a  
73 consistent assimilation and modeling procedure that incorporates all the available observed  
74 conditions obtained from conventional and satellite information from 1948 to the present  
75 (Kalnay et al. 1996). We used NCEP/NCAR reanalysis daily geopotential height (GPH) and  
76 wind data from the years 1948 to 2016. The NCEP/NCAR data assimilation uses a 3D-



77 variational analysis scheme with 28 pressure levels and triangular truncation of 62 waves  
78 (horizontal resolution of 200m). Both GPH and temperature at the chosen standard levels are  
79 described as class output variables (Kalnay et al. 1996) i.e. they are strongly influenced by  
80 observed data. Only the Indian summer monsoon months (June, July, and August,  
81 September) containing gridded daily data were considered in this study. The NCEP/NCAR  
82 reanalysis data had a spatial resolution of  $2.5^\circ$ . The seasonal values are estimated from daily  
83 data. To identify the spatial and temporal variations of the anticyclone centres, we used the  
84 monthly mean values of the GPH and the zonal wind component. The quality of NCEP GPH  
85 reanalysis data can be found from Bromwich et al., (2007).

## 86 **2.2. IMD Gridded Precipitation Data**

87 The India Meteorological Department (IMD) high-resolution ( $0.25^\circ \times 0.25^\circ$ ) gridded  
88 precipitation data is used to identify the wet and dry spells during June, July and August  
89 months from 1901-2016. This precipitation data has been validated extensively with  
90 observational and reanalysis data sets and displays very good correlation (Kishore et al.,  
91 2016). For identification of active (or wet) and break (or dry) spells, we followed the similar  
92 procedure as described by Rajeevan et al. (2010) and Pai et al. (2016) over the monsoon core  
93 zone ( $18^\circ\text{N}$ - $28^\circ\text{N}$ , and  $65^\circ\text{E}$ - $88^\circ\text{E}$ ). Data from 1948-2016 have been used.

## 94 **2.3. GNSS Radio Occultation (RO) Data**

95 We also used the Global Navigation Satellite System (GNSS) RO data for investigating  
96 the temperature anomaly. The basic measurement principle of RO exploits the atmosphere-  
97 induced phase delay in the GNSS signals, which are recorded in the low earth orbiting  
98 satellite. This technique provides vertical profiles of refractivity, density, pressure,  
99 temperature, and water vapour (Kursinski et al., 1997). The temperature profiles from this  
100 technique are available with low horizontal ( $\sim 200$ - $300$  km) and high vertical resolutions ( $0.5$ -  
101  $15$  km) with accuracy of  $<0.5$  K. We used the CHALLENGING Minisatellite Payload (CHAMP)



102 and Constellation Observing System for Meteorology, Ionosphere, and Climate (COSMIC)  
103 covering the period from 2002 to 2016.

104 The CHAMP satellite was launched on 15 July 2000 in to a circular orbit by Germany  
105 to measure the Earth's gravity and magnetic field and to provide global RO soundings  
106 (Wickert et al. 2001). About ~230 RO profiles per day were measured by the CHAMP  
107 payload since 2002. The CHAMP payload was solely designed to track the setting  
108 occultations, and the RO event gets terminated when the signal is lost, which results in a  
109 decrease in the number of occultations with a decreasing altitude (Beyerle et al. 2006). This  
110 receiver measures the phase delay of radio wave signals that are occulted by the Earth's  
111 atmosphere. From this phase delay, it is possible to retrieve the bending angle and refractivity  
112 vertical profiles. The CHAMP data was available from 19 May 2001 to 5 October 2009.

113 COSMIC consists of a constellation of 6 satellites, which was launched in April 2006  
114 to a circular, 72° inclination orbit at a 512 km altitude capable of receiving signals from the  
115 Global Positioning System (GPS) (Anthes et al., 2008). Compared to previous satellites,  
116 COSMIC satellites employed an open loop mode, which can track both the rising and setting  
117 of occultations (Schreiner et al. 2007). The open-loop tracking technique significantly  
118 reduces the GPS RO inversion biases by eliminating tracking errors (Sokolovskiy et al.  
119 2006). The COSMIC temperature profiles display a very good agreement with radiosonde  
120 data, reanalyses, and models (Rao et al., 2009; Kishore et al., 2011; Kishore et al., 2016). We  
121 derived the cold point tropopause altitude/temperature over the ASMA region as discussed by  
122 Ratnam et al. (2014) and Ravindrababu et al. (2015). Both the CHAMP and COSMIC data  
123 were obtained from COSMIC Data Analysis and Archive Center (CDAAC) (<https://cdaac->  
124 [www.cosmic.ucar.edu/cdaac/products.html](http://www.cosmic.ucar.edu/cdaac/products.html)).

125

### 126 **3. Results and Discussion**



### 127 **3.1. Variability of the Anticyclone**

128 Climatological spatial variability of the GPH along wind vectors at 100 hPa during June,  
129 July, August and September months from NCEP reanalysis data is shown in Figure 1(a, b, c  
130 & d). The anticyclone circulation is clearly depicted during June, July, August and September  
131 by wind vectors (Figure 1). During the month of September and June the values of GPH are  
132 low compared to July and August which represents the spatial extent of the anticyclone. The  
133 spatial extent and intensity of anticyclone are greater during July compared to the intensities  
134 present during other months. During July and August, the anticyclone extends from the  
135 Middle East to East Asia. The spatial extent of anticyclone circulation is clearly evident in the  
136 grid 15°N-45°N; 30°E-120°E at 100 hPa level and the climatological averaged values of GPH  
137 varies from 16.5-17 km in NCEP reanalysis during 1948-2016. Using the modified potential  
138 vorticity equation, Randel et al. (2006) showed the spatial variation of anticyclone where  
139 GPH values are stationary in the range of 16.75-16.9 km. Similarly, Park et al. (2007) showed  
140 the anticyclone structure from the strongest wind at 100 hPa through streamline function.  
141 Bian et al. (2012) reported the spatial variability of anticyclone using 16.77 km and 16.90 km  
142 in the GPH contour as the lower and the upper boundary, respectively. Thus, these  
143 empirically selected GPH values represent anticyclone boundaries. Therefore, in this present  
144 study, we have chosen the values from 16.75 to 16.9 km to investigate the spatial features of  
145 the anticyclone and the resultant picture is depicted in Figure 1(e, f, g & h). The spatial extent  
146 and existence of anticyclone is highly prominent during July and August compared to June.  
147 During the September month, the GPH values in the range 16.75-16.9 km are not present.  
148 Therefore, we considered the average of July and August GPH from 1948-2016 for further  
149 analysis as shown in Figure S1. The core region and the spatial extent of the anticyclone are  
150 clearly evident from Figure S1. The core region of anticyclone shows bimodal distribution  
151 i.e. one core located at the south-western flank of the Himalayas and another over Iran. The



152 core region over the south-western flank of Himalayas is due to large scale updraft, which is  
153 caused by the moist energy over Indo-Gangetic plain, heating of Tibetan plateau, and the  
154 orographic forcing of the Himalayas. Severe heating over Arabian Peninsula supports the  
155 formation of the mid-tropospheric anticyclone in the west. This anticyclone can merge  
156 intermittently within ASMA. It is also observed that the spatial extent of anticyclone varies  
157 drastically at different temporal scales. Therefore, seasonal variation is much more  
158 pronounced.

159 The decadal variation of the anticyclone is studied with respect to the spatial  
160 variability. Figure 2 shows the decadal spatial variation of the anticyclone with reference to  
161 the years 1951-1960. The significant difference in the decadal variation is noticed from  
162 Figure 2. The edges (east, north, and west) of the anticyclone undergo drastic changes during  
163 the period 1961-1970. In case of 1971-1980 period, except for a small portion in the east, the  
164 whole anticyclone shows drastic changes. During the decade 1971-1980, the recorded GPH  
165 values in anticyclone are lower by  $\sim 25$  m when compared to the values in 1951-1960. This  
166 feature is quite opposite during 1981-1990 where high values ( $\sim 30$  m) are observed compared  
167 to those in the reference period. The GPH difference is significant over the west, northeast  
168 and southern regions of the anticyclone during the 1991-2000 period. Similar changes are  
169 observed during 2001-2010. Compared to all the decadal differences, 2011-2016 shows a  
170 completely different picture. The changes are only in the western and north-eastern corner,  
171 whereas other parts of the anticyclone do not show any change. From this analysis, we  
172 observed significant changes in the anticyclone even from one decade to another, which can  
173 result in a change in chemical and dynamical changes over this region.

174 Further, the spatial distribution of trends is estimated during the years 1948-2016 by  
175 using robust regression analysis and is displayed in Figure 3. Spatially, the anticyclone trend  
176 shows two distinct pictures. The edges on all side of the anticyclone undergo noticeable



177 changes compared to the core region. The northern side of the anticyclone shows reduction  
178 (~30 m) in the strength whereas the southern part illustrates increases in strength. Therefore,  
179 in order to understand the asymmetry in the anticyclone variability, we have divided the  
180 anticyclone region into 4 different sectors as shown in Figure 4 based on the peak values of  
181 GPH along longitude and latitude cross-sections. The center values of GPH are located at  
182 70°E longitude and 32.5°N Latitude. The four sectors can be divided as South-East (SE)  
183 (22.5°N-32.5°N), North-East (NE) (32.5°N-40°N) in the longitude band of 70°E-120°E,  
184 South-West (SW) (22.5°N-32.5°N), and North-West (NW) (32.5°N-40°N) at the 20°E-70°E  
185 longitude range. The average time series (July and August) of zonal wind anomalies in these  
186 sectors from 1948-2016 are shown in Figure 5. The zonal wind shows a clearly increasing  
187 trend in all the sectors. From 1948 to 1980 the zonal wind anomalies are easterlies and later  
188 on, clear shift is noticed towards the westerlies. This represents that the westerlies are more  
189 dominant in recent decades with a strong increase in magnitude. The change is highly  
190 significant in the north-west and north-east sectors with a magnitude variability of 10 m/s  
191 from 1948-2016 whereas it is 5 m/s in the south-east and south-west sectors. It is to be noted  
192 that the winds in the anticyclone will not be contaminated with the tropical easterly jet  
193 persisting during the monsoon season as their cores are well separated. One is located in the  
194 northern part and the other in the southern part of India. In addition, we estimated the strength  
195 of the anticyclone during the monsoon season by using a difference in the zonal wind  
196 between the northern (30°N-40°N) and southern (10°N-20°N) flanks of the anticyclone,  
197 which is depicted in Figure 5e. A significant increase in the strength of the anticyclone is  
198 noticed from Figure 5e at a rate of 0.184 m/s per year (12 m/s from 1948-2018).

199         It is well known that the Indian monsoon rainfall varies at different time scales i.e.  
200 daily, sub-seasonal, interannual, decadal and centennial scales. Precipitation during the  
201 monsoon varies from intra-seasonal scales between active (good rainfall) and break (little



202 rainfall) spells. Any small change in the precipitation pattern will affect the anticyclone due  
203 to the thermodynamics involved in rainfall. In this study, we also investigated the anticyclone  
204 variability (during the active and break spells of the Indian monsoon. The active and break  
205 spells were identified in July and August by using the high resolution gridded ( $0.25^\circ \times 0.25^\circ$ )  
206 rainfall data from 1948 to 2016 as defined by Pai et al. (2010).

207         The number of active and break days is derived from the precipitation data shown in  
208 Figure S2 (a & b). Daily GPH, temperature, and zonal wind are taken from NCEP reanalysis  
209 whereas the tropopause altitude is derived from the GNSS RO data for active and break days.  
210 The anticyclone structure during active (red line) and break (blue line) days are shown in  
211 Figure 6a. Two interesting aspects of the anticyclone variability can be noticed between  
212 active and break days. One aspect is the extent of the anticyclone is large during active days  
213 compared to break days and another is the existence of two cell structures in the anticyclone  
214 core region during active days. The extent is large in the eastern and northern side in active  
215 days. The zonal (meridional) cross section of temperature (color shade), zonal wind (contour  
216 lines) difference between active and break phase averaged in the longitude band of  $80^\circ\text{E}$ - $90^\circ\text{E}$   
217 (latitude band of  $30^\circ\text{N}$ - $40^\circ\text{N}$ ) along with cold point tropopause for active and break days is  
218 illustrated in Figures 6b & 6c. During active days, temperature shows cooling in tropical  
219 latitudes whereas it shows warming in the mid-latitudes from surface to tropopause.  
220 Significant warming is observed during the active days in the mid-troposphere over the  
221 Tibetan Plateau and its northern side. Westerly (easterly) winds exist over the warmer and  
222 cooler regions. The warm temperature anomalies stretch from 1.5 to 12 km in between  $25^\circ\text{N}$   
223 and  $60^\circ\text{N}$ . The tropopause altitude is low (high) during the active (break) phase of Indian  
224 monsoon as show in Figure 6b. The meridional cross-section of temperature anomalies  
225 displays significant warming from  $\sim 1.5$  to 8 km over the Indian region. The tropopause  
226 altitude exemplifies random variability in the meridional cross section.



227 As discussed previously, the anticyclone circulation is significant during the months  
228 of July and August when most of the precipitation occurs over India (Basha et al., 2015;  
229 Kishore et al., 2015). The influence of strong and weak monsoon years will have a drastic  
230 impact on anticyclone circulation. In order to understand these changes, we have divided the  
231 years into strong and weak monsoon years based on gridded precipitation data over the  
232 domain 5°N-30°N and 70°E-95°E from the years 1948-2016. This region is known to have  
233 heavy precipitation and orographic forcing, which helps transport of water vapour through  
234 deep convection to UTLS (Houze et al., 2007; Medina et al., 2010; Pan et al., 2016). The  
235 detrended precipitation represents the strong and weak monsoon years. Years with positive  
236 (negative) values of precipitation shows the strong (weak) monsoon years as shown in Figure  
237 S2b. Further, we have divided the GPH, temperature at 100 hPa tropopause altitude based on  
238 strong and weak monsoon years. The composite of mean distribution of anticyclone  
239 circulation during strong and weak monsoon years is shown in Figure 7a. The circulation  
240 expands on the eastern and western sides of the anticyclone during the weak monsoon (blue  
241 line) years. The core of the anticyclone is significant during strong monsoon years. Clear eye  
242 structure is observed on the right (left) side of the anticyclone in the core region during the  
243 strong (weak) monsoon years. The composite mean difference of temperature and zonal wind  
244 between the strong and weak monsoon years along with tropopause altitude averaged in the  
245 longitude range of 80-85°E is shown in Figure 7b. The warmest temperature anomalies are  
246 observed over the Tibetan Plateau. Positive (warm) temperature anomalies exactly above the  
247 Tibetan Plateau (11 km) and negative (cooling) on both sides are noticed in the lower  
248 troposphere from Figure 7b. Strong easterlies (westerlies) winds are observed on the left  
249 (right) side of the Tibetan Plateau. The whole Tibetan Plateau acts as a barrier that drives the  
250 cold air to upper altitudes during strong monsoon years. Strong anticyclone circulation with  
251 strong westerlies at 35°N and easterlies on both sides with elevated tropopause represent the



252 impacts of the strong monsoon vertically above the anticyclone. The raising motion over East  
253 Asia excited by the local heating of the Tibetan Plateau links to the single stretch vertically.  
254 The longitude and altitude cross-section of temperature and wind anomalies shown in Figure  
255 7c are averaged between a latitude band of 35-40°N. Positive temperature anomalies are  
256 observed from the surface to 12 km in the longitudes 60-80°E and stretch towards the west.  
257 This clearly demonstrates that a large scale ascent develops over the Asian monsoon region.  
258 The tropopause altitude is high (low) during strong vertical motion and heavy precipitation  
259 found over the region similar to that reported by Lau et al. (2018). The transport processes  
260 from the boundary layer to the tropopause occurs on the east side of the anticyclone i.e.  
261 southern flank of Tibetan Plateau, northeast India and the head of the Bay of Bengal. This  
262 result is consistent with the previous studies by Bergman et al. (2013).

263 ENSO typically shows the strongest signal in boreal winter, but it can affect the  
264 atmospheric circulation and constituent distributions until the next autumn. It is well-known  
265 that strong ENSO events have a significant influence on tropical upwelling and STE. This  
266 change can impact the distribution of composition and structure of UTLS region. In the  
267 UTLS region, the tropopause responds to the annual and interannual variability associated  
268 with ENSO (Trenberth, 1990) and QBO (Baldwin et al., 2001). Several studies have been  
269 focused on the effects of the different impacts of El Niño on tropopause and lower  
270 stratosphere (Hu and Pan, 2009; Zubiaurre and Calvo, 2012; Xie et al., 2012). In the present  
271 study, we have investigated the changes associated with strong ENSO events with the  
272 anticyclone circulation and tropical upwelling during July and August. Therefore, we have  
273 also separated the GPH for the strongest El Niño (1958, 1966, 1973, 1983, 1988, 1992, 1998,  
274 and 2015) and La Niña (1974, 1976, 1989, 1999, 2000, 2008, and 2011) years to verify the  
275 change in the circulation pattern of the anticyclone. For this we have chosen July and August  
276 GPH data at 100hPa as shown in Figure 8. The red and blue colors indicate the composite of



277 the La Niña and El Niño circulation. During the El Niño, the anticyclone circulation is  
278 stronger and extends over the La Niña at 100 hPa as shown in the Figure 8a. On the eastern  
279 and southern sides of the anticyclone, the expansion is more during the La Niña years. The  
280 warm temperature with strong westerlies in the latitude band of 43°N-55°N is observed  
281 during the El Niño as shown in Figure 8b (Lau et al., 2018). The cooling impact is significant  
282 over the Tibetan Plateau during La Niña events compared to El Niño events. Significant  
283 cooling is observed over the Tibetan Plateau and distributes towards tropical latitudes  
284 between 600-100 hPa. The zonal wind shows a convergence of easterly winds over the  
285 Tibetan Plateau from the mid to the upper tropospheric region. In the right side of the Tibetan  
286 Plateau there exist strong westerly winds from the surface to the tropopause altitudes with  
287 strong warming. The meridional cross-section of temperature and the zonal wind difference  
288 between La Niña and El Niño is shown in Figure 8c. Significant cooling is observed during  
289 La Niña in the longitude band of 80°E-100°E with strong easterlies from the surface to the  
290 tropopause. From this analysis, it is clear that the Indian summer monsoon variability has a  
291 significant impact on ASMA, and it is necessary to consider the different phases of monsoon  
292 while dealing with UTLS pollutants. In addition, we have investigated the zonal mean  
293 vertical cross-section in the longitude band of 50-60°E, which represents the Iranian Mode.  
294 Figure S3 depicts the difference between active and break phases, strong and weak monsoon  
295 years, and La Niño and El Niño years along with the tropopause altitude. Significant warming  
296 is observed during La Niña years and strong monsoon years compared to the active phase of  
297 the Indian monsoon in the troposphere. Compared to the Tibetan mode, the Iranian mode  
298 warming is less. The tropopause altitude is slightly higher during the active phase of the  
299 Indian monsoon, strong monsoon years and La Niña years. A moderate increase in  
300 tropopause from equator to 40°N is observed and decreases drastically afterwards.

#### 301 4. Summary and Conclusions



302 Several authors discussed the interannual and decadal variability of pollutants and tracers  
303 in the ASMA region from the model, observational and reanalysis data sets (Kunze et al.,  
304 2016; Santee et al., 2017; Yuan et al., 2019). In this present study, we have investigated the  
305 spatial variability, trends of the anticyclone and the influence of Indian monsoon activity i.e.  
306 active and break days, strong and weak monsoon years, and strong La Niña and El Niño years  
307 on ASMA using long-term reanalysis and observational data sets that were not investigated  
308 earlier. We have considered the GPH values from 16.75 km to 16.9 km, which represents the  
309 spatial structure of anticyclone at 100 hPa in this study. Our analysis shows that the spatial  
310 (magnitude) of the anticyclone structure is very large (strong) during July followed by  
311 August whereas it is very weak in June at 100 hPa. The bimodal distribution (Tibetan and  
312 Iranian modes) of the anticyclone is clearly observed during the month of July which is not  
313 present during other months (June and August). The anticyclone variability undergoes  
314 significant decadal variations from one decade to another. The edges of ASMA changes  
315 drastically compared to the core of anticyclone. However, there are significant spatial  
316 differences in the structure of the anticyclone at 100 hPa. The anticyclone undergoes a  
317 decreasing trend on the northern side whereas an increasing trend on the western part. A  
318 significant increasing trend is observed in the spatially averaged zonal wind in four different  
319 sectors (Figure 5). The zonal wind anomalies illustrate easterlies from 1948 to 1980 and  
320 westerlies thereafter. In the recent decade the westerlies are significant in the anticyclone  
321 region at 100 hPa. The change is significant in the north-western and north-eastern sectors  
322 with a magnitude variability of 10 m/s from 1948-2016 whereas it is 5 m/s in the south-  
323 eastern and south-western sectors. The strength of the anticyclone increases with a rate of  
324 0.184 m/s per year (12 m/s from 1948-2016) in the anticyclone region (Figure 5e). Yuan et al.  
325 (2019) also reported the increasing trend in the strength of the anticyclone by considering the  
326 MERRA 2 reanalysis data from 2001-2015.



327 Further, we have investigated the Indian monsoon influence on the anticyclone region.  
328 Our results reveal that the spatial extent of the anticyclone expands during the active phase of  
329 the Indian monsoon, the strong monsoon years and during strong La Niña years on the  
330 northern and eastern sides. During these events, the bimodal distribution (Tibetan and Iranian  
331 modes) of the anticyclone is noticed. A similar expansion of the anticyclone is noticed during  
332 strong monsoon years from MERRA2 data by Yuan et al. (2019). However, the ASMA  
333 boundaries are not always well defined in all the events. The zonal mean cross-section of  
334 temperature shows significant warming over the Tibetan Plateau and from the surface to 12  
335 km during the active phase of the Indian monsoon, the strong monsoon years, and the strong  
336 La Niña years. Similarly, the rise of tropopause during the active phase of the Indian  
337 monsoon, the strong monsoon years and the strong La Niña years is noticed. Since the  
338 Tibetan Plateau acts as a strong heat source in summer with the strongest heating layer lying  
339 in the lower layers, the thermal adaptation results in a shallow and weak cyclonic circulation  
340 near the surface, and a deep and strong anti-cyclonic circulation above it. During summer, the  
341 Tibetan Plateau acts as a strong heat source, which influences the whole UTLS region. The  
342 warm ascending air above will pull the air from below; the surrounding air in the lower  
343 troposphere converges towards the Tibetan Plateau area and climbs up the heating sloping  
344 surfaces (Bergman et al., 2013; Garny and Randel, 2016). Significant warming is observed  
345 over the Tibetan Plateau, which represents the strong transport of pollutants into the  
346 tropopause during the active phase of the Indian monsoon, the strong monsoon years, and the  
347 strong La Niña years. Pan et al. (2016) reported the transport of carbon monoxide through the  
348 southern flank of the Tibetan Plateau from the model analysis. The above mentioned results  
349 indicate that the high mountain regions play a significant role in elevated heat sources during  
350 the formation and maintenance of the anticyclones over Asia. It emphasizes the role of the  
351 thermal forcing of the Tibetan Plateau on the temporal and the spatial evolution of the South



352 Asian High. Lau et al. (2018) showed that the transport of the dust and pollutants from the  
353 Himalayas-Gangetic Plain and the Sichuan Basin.

354 Overall, we demonstrate the ASMA variability during different phases of the Indian  
355 monsoon. The uplifting of boundary layer pollutants to the tropopause level occurs primarily  
356 on the eastern side of the anticyclone, centered near the southern flank of the Tibetan Plateau,  
357 north-eastern India, Nepal, and north of the Bay of Bengal. However, a more detailed and a  
358 higher quality of dataset is needed to further understand the effects of the Tibetan Plateau on  
359 the transport of different tracers and pollutants to the UTLS region (Ravindrababu et al.,  
360 2019).

361  
362 *Data Availability.* The NCEP/NCAR reanalysis data are available from NOAA website  
363 (<https://www.esrl.noaa.gov/psd/data/gridded/data.ncep.reanalysis.pressure.html>). The  
364 COSMIC and CHAMP data is available from COSMIC CDAAC website. IMD gridded  
365 precipitation data is available at National Climate data center Pune, India. All the data used in  
366 the present study is available freely from the respective websites.

367 *Authors' Contributions.* GB and MVR conceived and designed the scientific questions  
368 investigated in the study. GB performed the analysis and wrote the draft in close cooperation  
369 with MVR. PK estimated the active and break spells of the Indian monsoon. All authors  
370 edited the paper.

371 *Competing Interests.* The authors declare that they have no competing financial interests.

372 *Acknowledgements.* We thank NCEP/NCAR reanalysis for providing reanalysis data. We  
373 thank CDAAC for production of COSMIC and CHAMP GPSRO data and IMD gridded  
374 precipitation data from National Climate data center Pune, India. This work was supported by  
375 National Atmospheric Research Laboratory, Department of Space, and India

376 **References**



- 377 Anthes, R. A., Bernhardt, P. A., Chen, Y., Cucurull, L., Dymond, K. F., Ector, D., Healy, S.  
378 B., Ho, S.-H., Hunt, D. C., Kuo, Y.-H., Liu, H., Manning, K., McCormick, C., Meehan, T.  
379 K., Randel, W. J., Rocken, C., Schreiner, W. S., Sokolovskiy, S. V., Syndergaard, S.,  
380 Thompson, D. C., Trenberth, K. E., Wee, T.-K., Yen, N. L., and Zeng, Z.: The  
381 COSMIC/Formosat/3 mission: Early results, *B. Am. Meteorol. Soc.*, 89, 313–333, 2008.  
382 Rao, D. N., Ratnam, M. V., Mehta, S., Nath, D., Ghouse Basha, S., Jagannadha Rao, V. V.  
383 M., Krishna Murthy, B. V., Tsuda, T., and Nakamura, K.: Validation of the COSMIC  
384 radio occultation data over Gadanki (13.48 N, 79.2 E): A tropical region, *Terr. Atmos.*  
385 *Ocean. Sci.*, 20, 59–70, doi:10.3319/TAO.2008.01.23.01(F3C), 2009.
- 386 Baldwin, M. P., Gray, L. J., Dunkerton, T. J., Hamilton, K., Haynes, P. H., Randel, W. J.,  
387 Holton, J. R., Alexander, M. J., Hirota, I., Horinouchi, T., Jones, D. B. A., Kinnerson, J.,  
388 S., Marquardt, C., Sato, K., and Takahashi, M.: The quasi-biennial oscillation, *Rev.*  
389 *Geophys.*, 39, 179–229, doi:10.1029/1999RG000073, 2001.
- 390 Basha, G., Kishore, P., Ratnam, M. V., Ouarda, T. B. M. J., Velicogna, I., and Tyler Sutterly, J.:  
391 Vertical and latitudinal variation of the intertropical convergence zone derived using GPS  
392 radio occultation measurements, *Remote Sensing of Environment*,  
393 <http://dx.doi.org/10.1016/j.rse.2015.03.024>, 2015.
- 394 Bergman, J. W., Fierli, F., Jensen, E. J., Honomichl, S., and Pan, L. L.: Boundary layer  
395 sources for the Asian anticyclone: Regional contributions to a vertical conduit, *J. Geophys.*  
396 *Res.*, 118, 2560–2575, <https://doi.org/10.1002/jgrd.50142>, 2013.
- 397 Beyerle, G., Schmidt, T., Wickert, J., Heise, S., Rotacher, M., Koenig-Langlo, G., and  
398 Lauritsen, K. B.: Observations and simulations of receiver-induced refractivity biases in  
399 GPS radio occultation, *J. Geophys. Res.*, 111, D12101, doi:10.1029/2005JD006673, 2006.



- 400 Bian, J., Pan, L. L., Paulik, L., Vömel, H., and Chen, H.: In situ water vapor and ozone  
401 measurements in Lhasa and Kunmin during the Asian summer monsoon, *Geophys. Res.*  
402 *Let.*, 39, L19808, doi:10.1029/2012GL052996, 2012.
- 403 Bromwich, D. H., Fogt, R. L., Hodges, K. I., and Walsh, J. E.: A tropospheric assessment of  
404 the ERA-40, NCEP, and JRA-25 global reanalyses in the polar regions, *J. Geophys. Res.-*  
405 *Atmos.*, 112, D10111, doi:10.1029/2006JD007859, 2007.
- 406 Fadnavis, S., Schultz, M. G., Semeniuk, K., Mahajan, A. S., Pozzoli, L., Sonbawne, S.,  
407 Ghude, S. D., Kiefer, M., and Eckert, E.: Trends in peroxyacetyl nitrate (PAN) in the  
408 upper troposphere and lower stratosphere over southern Asia during the summer monsoon  
409 season: regional impacts, *Atmos. Chem. Phys.*, 14, 12 725–12 743,  
410 <https://doi.org/10.5194/acp-14-12725-2014>, 2014.
- 411 Garny, H. and Randel, W. J.: Dynamic variability of the Asian monsoon anticyclone  
412 observed in potential vorticity and correlations with 5 tracer distributions, *J. Geophys.*  
413 *Res.*, 118, 13 421–13 433, <https://doi.org/10.1002/2013JD020908>, 2013.
- 414 Garny, H. and Randel, W. J.: Transport pathways from the Asian monsoon anticyclone to the  
415 stratosphere, *Atmos. Chem. Phys.*, 16, 2703–2718, [https://doi.org/10.5194/acp-16-2703-](https://doi.org/10.5194/acp-16-2703-2016)  
416 2016, 2016.
- 417 Glatthor, N., Höpfner, M., Stiller, G. P., von Clarmann, T., Funke, B., Lossow, S., Eckert, E.,  
418 Grabowski, U., Kellmann, S., Linden, A., Walker, K. A., and Wiecele, A.: Seasonal and  
419 interannual variations in HCN amounts in the upper troposphere and lower stratosphere  
420 observed by MIPAS, *Atmos. Chem. Phys.*, 15, 563–582, [https://doi.org/10.5194/acp-15-](https://doi.org/10.5194/acp-15-563-2015)  
421 563-2015, 2015.
- 422 Gottschaldt, K.-D., Schlager, H., Baumann, R., Cai, D. S., Eyring, V., Graf, P., Grewe, V.,  
423 Jöckel, P., Jurkat-Witschas, T., Voigt, C., Zahn, A., and Ziereis, H.: Dynamics and



- 424 composition of the Asian summer monsoon anticyclone, *Atmos. Chem. Phys.*, 18, 5655-  
425 5675, <https://doi.org/10.5194/acp-18-5655-2018>, 2018.
- 426 Hossaini, R., Chipperfield, M., Montzka, M. P., Rap, S. A., Dhomse, S., and Feng, W.:  
427 Efficiency of short-lived halogens at influencing climate through depletion of stratospheric  
428 ozone, *Nature Geoscience*, 8, 186–190, <https://doi.org/10.1038/ngeo2363>, 2015.
- 429 Hoskins, B. J., and Rodwell, M. J.: A model of the Asian summer monsoon, I: The global  
430 scale, *J. Atmos. Sci.*, 52, 1329–1340, 1995.
- 431 Highwood, E. J. and Hoskins, B. J.: The tropical tropopause, *Q. J. Roy. Meteor. Soc.*, 124,  
432 1579–1604, 1998.
- 433 Houze, R. A., Wilton, D. C., and Smull, B. F.: Monsoon convection in the Himalayan region  
434 as seen by the TRMM 345 Precipitation Radar, *Q. J. Roy. Meteor. Soc.*, 133, 1389-1411,  
435 [10.1002/qj.106](https://doi.org/10.1002/qj.106), 2007.
- 436 Hu, Y. and Pan, L.: Arctic stratospheric winter warming forced by observed SSTs, *Geophys.*  
437 *Res. Lett.*, 36, L11707, [doi:10.1029/2009GL037832](https://doi.org/10.1029/2009GL037832), 2009.
- 438 Kishore, P., Ratnam, M. V., Namboothiri, S., Velicogna, I., Basha, G., Jiang, J., Igarashi, K.,  
439 Rao, S., and Sivakumar, V.: Global (50° S–50° N) distribution of water vapor observed by  
440 COSMIC GPS RO: Comparison with GPS radiosonde, NCEP, ERAInterim, and JRA-25  
441 reanalysis data sets, *J. Atmos. Sol.-Terr. Phy.*, 73, 1849–1860,  
442 [doi:10.1016/j.jastp.2011.04.017](https://doi.org/10.1016/j.jastp.2011.04.017), 2011.
- 443 Kishore, P., Jyothi, S., Basha, G., Rao, S.V.B., Rajeevan, M., Velicogna, I., and Sutterley,  
444 T.C.: Precipitation climatology over India: validation with observations and reanalysis  
445 datasets and spatial trends. *ClimDyn* 121. [doi: 10.1007/s00382-015-2597-y](https://doi.org/10.1007/s00382-015-2597-y), 2015.
- 446 Kishore, P., Basha, G., VenkatRatnam, M., Velicogna, I., Ouarda, T. B. M. J., and Narayana  
447 Rao, D.: Evaluating CMIP5 models using GPS radio occultation COSMIC temperature in



- 448 UTLS region during 2006–2013: twenty-first century projection and trends, *Clim.*  
449 *Dynam.*, 47, 3253–3270, <https://doi.org/10.1007/s00382-016-3024-8>, 2016.
- 450 Kalnay, E., Kanamitsu, M., Kistler, R., Collins, W., Deaven, D., Gandin, L., Iredell, M.,  
451 Saha, D., White, G., Woollen, J., Zhu, Y., Chelliah, M., Ebisuzaki, W., Higgins, W.,  
452 Janowiak, J., Mo, K.C., Ropelewski, C., Wang, J., Leetma, A., Reynolds, R., and Dennis,  
453 J.: The NCEP/NCAR 40-years reanalysis project. *Bull. Am. Meteorol. Soc.* 77, 437–472.  
454 1996.
- 455 Kursinski, E. R., Hajj, G. A., Schofield, J. T., Linfield, R. P., and Hardy, K. R.: Observing  
456 Earth’s atmosphere with radio occultation measurements using the Global Positioning  
457 System, *J. Geophys. Res.-Atmos.*, 102, 23429–23465, 1997.
- 458 Kunze, M., Braesicke, P., Langematz, U., and Stiller, G.: Interannual variability of the boreal  
459 summer tropical UTLS in observations and CCMVal-2 simulations, *Atmos. Chem. Phys.*,  
460 16, 8695–8714, <https://doi.org/10.5194/acp-16-8695-2016>, 2016.
- 461 Lau, W.K.M., Cheng, Y., and Li, Z.: Origin, maintenance and variability of the Asian  
462 Tropopause Aerosol Layer (ATAL): Roles of monsoon dynamics. *Sci. Rep.* 2018, 8, 3960.
- 463 Medina, S., Houze, R. A., Kumar, A., and Niyogi, D.: Summer monsoon convection in the  
464 Himalayan region: terrain and land cover effects, *Q. J. Roy. Meteor. Soc.*, 136, 593–616,  
465 [10.1002/qj.601](https://doi.org/10.1002/qj.601), 2010.
- 466 Pai, D.S., Sridhar, L., and Ramesh Kumar, M.R.: Active and break events of Indian summer  
467 monsoon during 1901–2014. *ClimDyn* 46, 3921– 3939. [https://doi.org/10.1007/s00382-](https://doi.org/10.1007/s00382-015-2813-9)  
468 [015-2813-9](https://doi.org/10.1007/s00382-015-2813-9), 2016.
- 469 Pan, L. L., Honomichl, S. B., Kinnison, D. E., Abalos, M., Randel, W. J., Bergman, J. W.,  
470 and Bian, J.: Transport of chemical tracers from the boundary layer to stratosphere  
471 associated with the dynamics of the Asian summer monsoon, *J. Geophys. Res. Atmos.*,  
472 121, 14159–14174, [10.1002/2016JD025616](https://doi.org/10.1002/2016JD025616), 2016.



- 473 Park, M., Randel, W. J., Gettleman, A., Massie, S. T., and Jiang, J. H.: Transport above the  
474 Asian summer monsoon anticyclone inferred from Aura Microwave Limb Sounder tracers,  
475 J. Geophys. Res., 112, D16309, <https://doi.org/10.1029/2006JD008294>, 2007.
- 476 Rajeevan, M., Gadgil, S., and Bhate, J.: Active and break spells of the Indian summer  
477 monsoon, J. Earth Syst. Sci., 119, 229–247, doi:[10.1007/s12040-010-0019-4](https://doi.org/10.1007/s12040-010-0019-4), 2010.
- 478 Randel, W. J., and Park, M.: Deep convective influence on the Asian summer monsoon  
479 anticyclone and associated tracer variability observed with Atmospheric Infrared Sounder  
480 (AIRS), J. Geophys. Res., 111, D12314, <https://doi.org/10.1029/2005JD006490>, 2006
- 481 Rao, D. N., Ratnam, M. V., Mehta, S., Nath, D., Ghose Basha, S., Jagannadha Rao, V. V.  
482 M., Krishna Murthy, B. V., Tsuda, T., and Nakamura, K.: Validation of the COSMIC  
483 radio occultation data over Gadanki (13.48 N, 79.2 E): A tropical region, Terr. Atmos.  
484 Ocean. Sci., 20, 59–70, doi:[10.3319/TAO.2008.01.23.01\(F3C\)](https://doi.org/10.3319/TAO.2008.01.23.01(F3C)), 2009.
- 485 Ratnam, M. V., Sunilkumar, S., Parameswaran, K., Murthy, B. K., Ramkumar, G., Rajeev,  
486 K., Basha, G., Babu, S. R., Muhsin, M., and Mishra, M. K.: Tropical tropopause dynamics  
487 (TTD) campaigns over Indian region: An overview, J. Atmos. Sol.-Terr. Phys., 121, 229–  
488 239, 2014
- 489 RavindraBabu, S., VenkatRatnam, M., Basha, G., Krishnamurthy, B. V., and  
490 Venkateswararao, B.: Effect of tropical cyclones on the tropical tropopause parameters  
491 observed using COSMIC GPS RO data, Atmos. Chem. Phys., 15, 10239–10249,  
492 doi:[10.5194/acp-15-10239-2015](https://doi.org/10.5194/acp-15-10239-2015), 2015.
- 493 Ravindrababu, S., Ratnam, M.V., Basha, G., Liou, Y.-A., Reddy, N.N.: Large Anomalies in  
494 the Tropical Upper Troposphere Lower Stratosphere (UTLS) Trace Gases Observed  
495 during the Extreme 2015–16 El Niño Event by Using Satellite Measurements. *Remote*  
496 *Sens.* 2019, 11(6), 687; <https://doi.org/10.3390/rs11060687>, 2019.



- 497 Riese, M., Ploeger, F., Rap, A., Vogel, B., Konopka, P., Dameris, M., and Forster, P.: Impact  
498 of uncertainties in atmospheric mixing on simulated UTLS composition and related  
499 radiative effects, *J. Geophys. Res.*, 117, D16305, <https://doi.org/10.1029/2012JD017751>,  
500 2012.
- 501 Santee, M. L., Manney, G. L., Livesey, N. J., Schwartz, M. J., Neu, J. L., and Read, W. G.: A  
502 comprehensive overview of the climatological composition of the Asian summer monsoon  
503 anticyclone based on 10 years of Aura Microwave Limb Sounder measurements, *J.*  
504 *Geophys. Res.-Atmos.*, 122, 5491– 5514, <https://doi.org/10.1002/2016JD026408>, 2017
- 505 Schreiner, W., Rocken, C., Sokolovskiy, S., Syndergaard, S., and Hunt, D.: Estimates of the  
506 precision of GPS radio occultations from the COSMIC/FORMOSAT-3 mission, *Geophys.*  
507 *Res. Lett.*, 34, L04808, doi:10.1029/2006GL027557, 2007.
- 508 Sokolovskiy, S. V., Kuo, Y.-H., Rocken, C., Schreiner, W. S., Hunt, D., and Anthes, R. A.:  
509 Monitoring the atmospheric boundary layer by GPS radio occultation signals recorded in  
510 the open-loop mode, *Geophys. Res. Lett.*, 33, L12813, doi:10.1029/2006GL025955, 2006.
- 511 Solomon, S., Rosenlof, K., Portmann, R., Daniel, J., Davis, S., Sanford, T., and Plattner, G.-  
512 K.: Contributions of stratospheric water vapor to 5 decadal changes in the rate of global  
513 warming, *Science*, 327, 1219–1223, <https://doi.org/10.1126/science.1182488>, 2010
- 514 Tissier, A.-S., and Legras, B.: Convective sources of trajectories traversing the tropical  
515 tropopause layer, *Atmos. Chem. Phys.*, 16, 3383–3398, doi:10.5194/acp-16-3383-2016,  
516 2016.
- 517 Trenberth, K. E.: Recent observed interdecadal climate changes in the Northern Hemisphere,  
518 *B. Am. Meteorol. Soc.*, 71, 988–993, doi:10.1175/1520-0477(1990)0712.0.CO;2, 1990.
- 519 Vernier, J. P., Fairlie, T. D., Natarajan, M., Wienhold, F. G., Bian, J., Martinsson, B. G.,  
520 Crumeyrolle, S., Thomason, L.W., and Bedka, K. M.: Increase in upper tropospheric and



- 521 lower stratospheric aerosol levels and its potential connection with Asian pollution, J.  
522 Geophys. Res., <https://doi.org/10.1002/2014JD022372>, 2015
- 523 Vogel, B., Günther, G., Müller, R., Groß, J.-U., Afchine, A., Bozem, H., Hoor, P., Krämer,  
524 M., Müller, S., Riese, M., Rolf, C., Spelten, N., Stiller, G. P., Ungermann, J., and Zahn,  
525 A.: Long-range transport pathways of tropospheric source gases originating in Asia into  
526 the northern lower stratosphere during the Asian monsoon season 2012, Atmos. Chem.  
527 Phys., 16, 15 301–15 325, <https://doi.org/10.5194/acp-16-15301-2016>, 2016.
- 528 Vogel, B., Günther, G., Müller, R., Groß, J.-U., and Riese, M.: Impact of different Asian  
529 source regions on the composition of the Asian monsoon anticyclone and of the  
530 extratropical lowermost stratosphere, Atmos. Chem. Phys., 15, 13 699–13 716,  
531 <https://doi.org/10.5194/acp15-13699-2015>, [http://www.atmos-chem-](http://www.atmos-chem-phys.net/15/13699/2015/)  
532 [phys.net/15/13699/2015/](http://www.atmos-chem-phys.net/15/13699/2015/), 2015.
- 533 Wickert, J., Reigber, C., Beyerle, G., König, R., Marquardt, C., Schmidt, T., Grunwaldt, L.,  
534 Galas, R., Meehan, T. K., Melbourne, W. G., and Hocke, K.: Atmosphere sounding by  
535 GPS radio occultation: First results from CHAMP, Geophys. Res. Lett., 28, 3263–3266,  
536 2001.
- 537 Xie, F., Li, J., Tian, W., Feng, J., and Huo, Y.: Signals of El Niño Modoki in the tropical  
538 tropopause layer and stratosphere, Atmos. Chem. Phys., 12, 5259–5273,  
539 <https://doi.org/10.5194/acp-12-5259-2012>, 2012.
- 540 Yan, R.-C., Bian, J.-C., and Fan, Q.-J.: The impact of the South Asia high bimodality on the  
541 chemical composition of the upper troposphere and lower stratosphere, Atmos. Ocean. Sci.  
542 Lett., 4, 229–234, 2011.
- 543 Yuan, C., Lau, W. K. M., Li, Z., and Cribb, M.: Relationship between Asian monsoon  
544 strength and transport of surface aerosols to the Asian Tropopause Aerosol Layer (ATAL):



545 interannual variability and decadal changes, *Atmos. Chem. Phys.*, 19, 1901-1913,  
546 <https://doi.org/10.5194/acp-19-1901-2019>, 2019.

547 Zhang, Q., Wu, G., and Qian, Y.: The Bimodality of the 100 hPa South Asia High and its  
548 Relationship to the Climate Anomaly over East Asia in summer, *J. Meteorol. Soc. Jpn.*,  
549 80, 733–744, 2002.

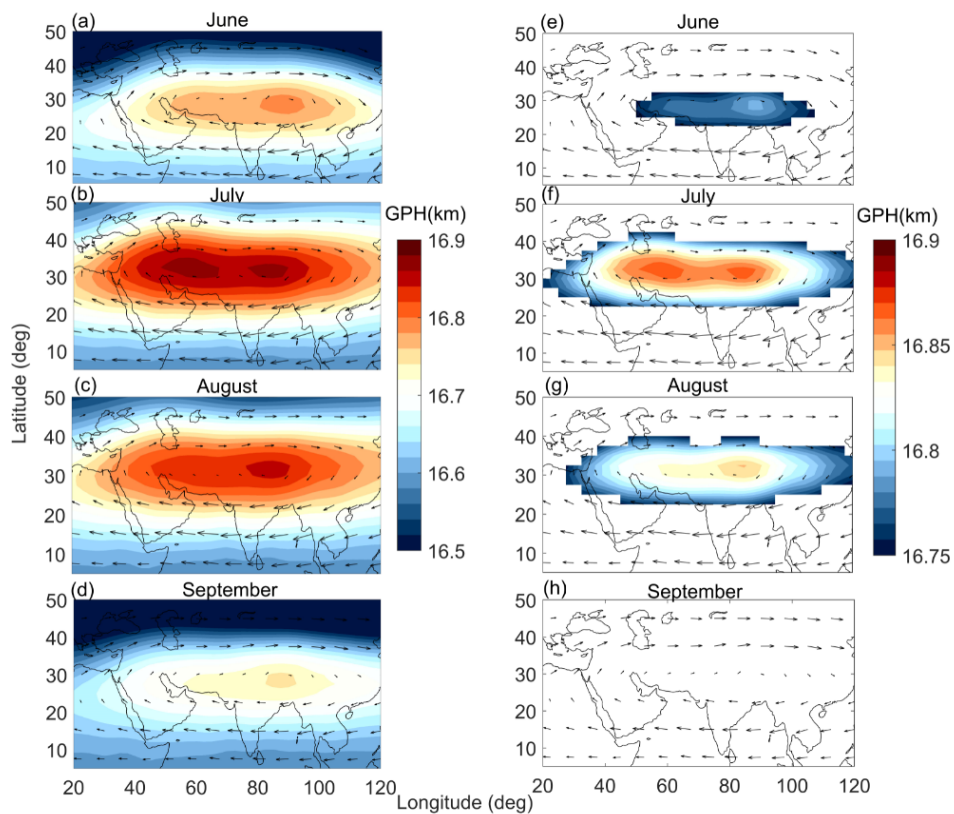
550 Zubiaurre, I., and Calvo, N.: The El Nino–Southern Oscillation (ENSO) Modoki signal in the  
551 stratosphere, *J. Geophys. Res.*, 117, D04104, doi:10.1029/2011JD016690, 2012.

552  
553  
554



555 **Figures**

556



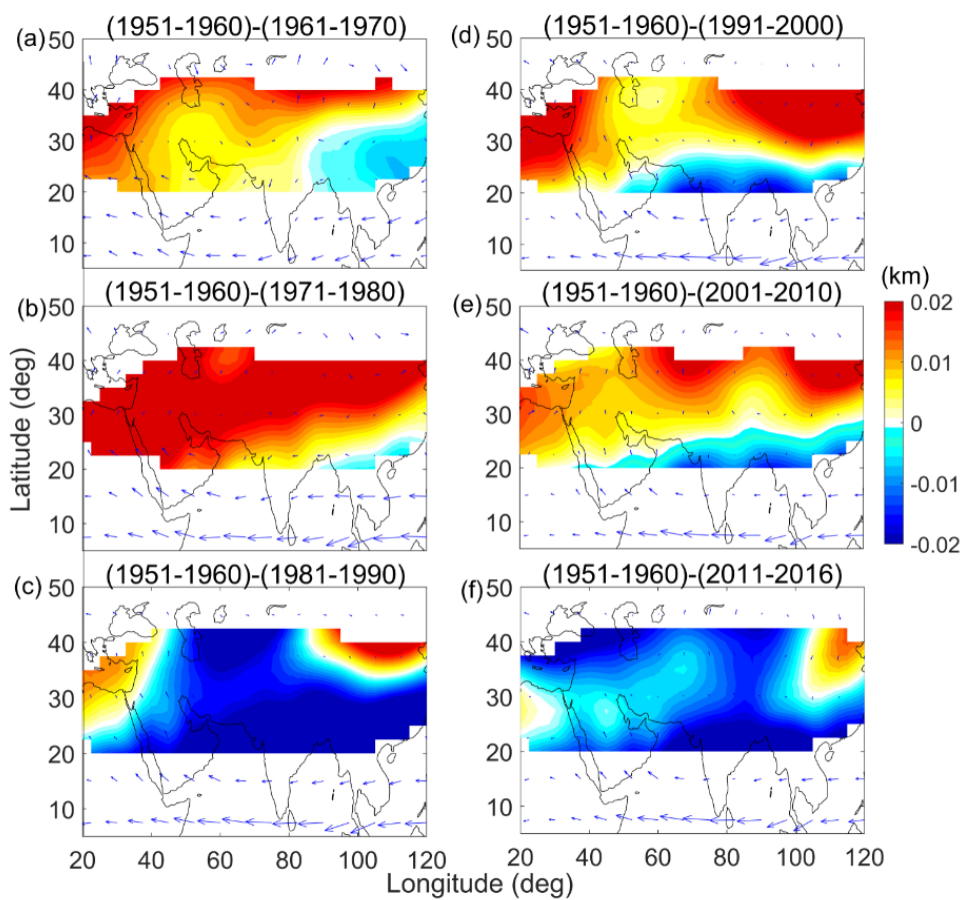
557

558 Figure 1. Spatial distribution of Geopotential Height (GPH) and wind vectors at 100 hPa  
559 during (a) June, (b) July, (c) August and (d) September from NCEP reanalysis data  
560 averaged from the year 1948-2016. The core of the anticyclone region was chosen based  
561 on the GPH values ranging from 16.75 to 16.9 km. The spatial extent and magnitude of the  
562 anticyclone after applying the GPH criteria for (e) June, (f) July, (g) August and (h),  
563 September.

564

565

566



567

568 Figure 2. Decadal variation of anticyclone obtained from GPH and wind vectors with  
569 reference to 1951-1960 period.

570

571

572

573

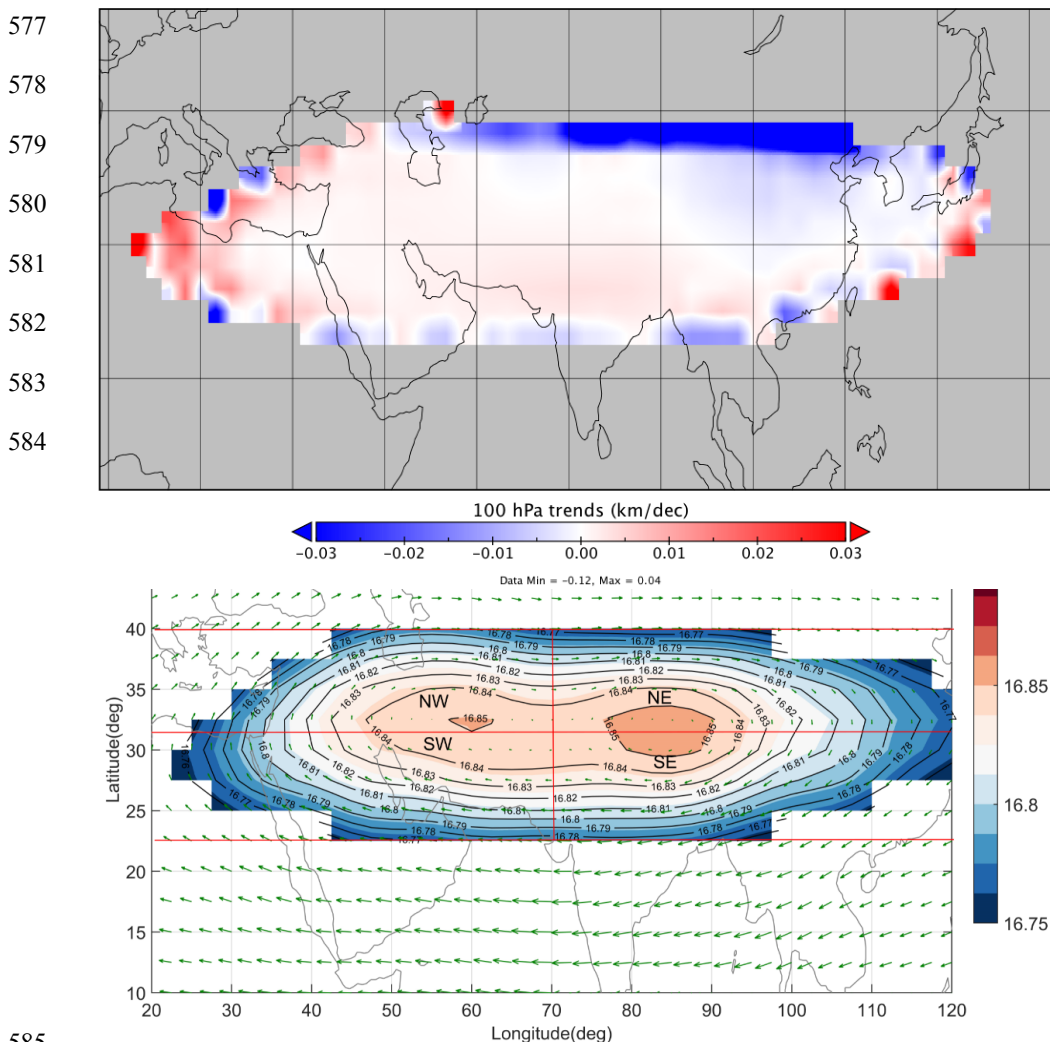
574

575

576

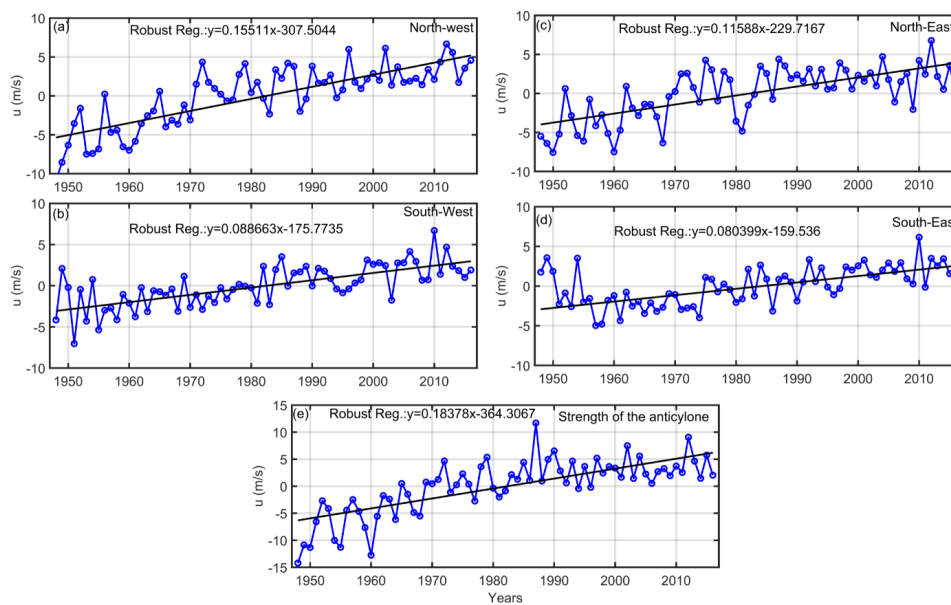


NCEP GHT 100 hPa JA trends (1948–2017)



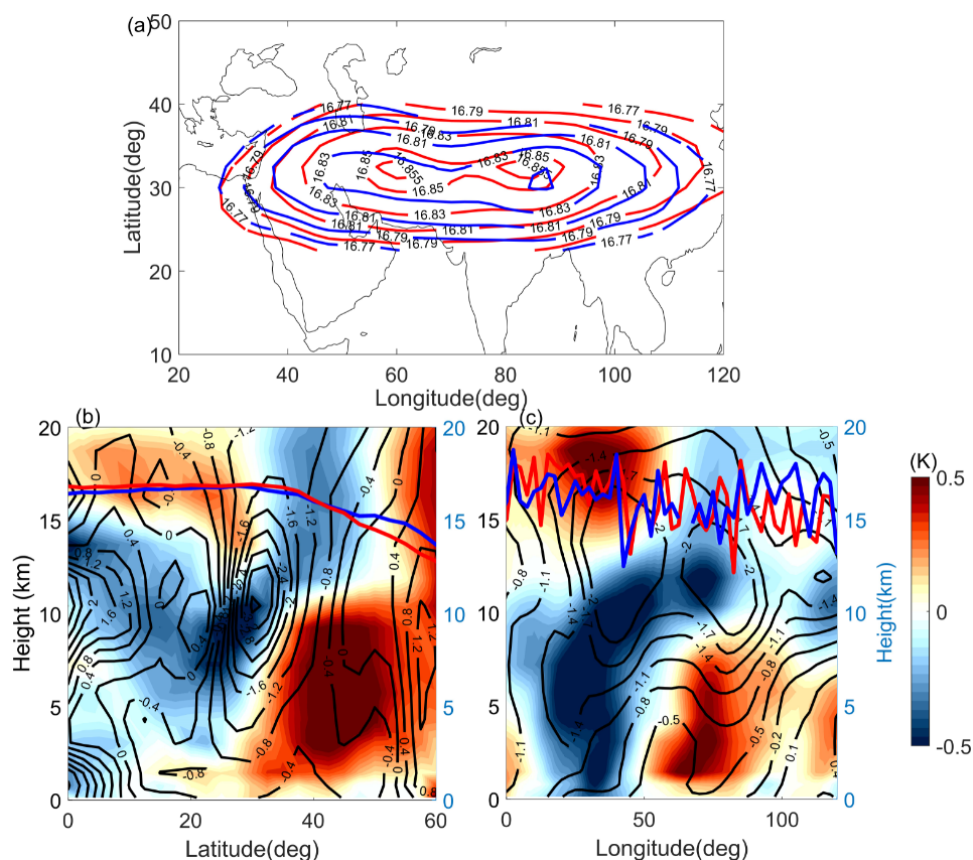
585

586 Figure 4. The climatological distribution of GPH (16.75 to 16.9 km) and wind vectors  
587 averaged during July and August from NCEP reanalysis data along with contour lines at  
588 100 hPa. The anticyclone region is further divided into 4 sectors based on peak values of  
589 GPH. The GPH values peak centres at  $32.5^{\circ}$  N in latitude and  $70^{\circ}$  E in longitude. The  
590 sectors are further divided into South-East (SE) ( $22.5^{\circ}$ N- $32.5^{\circ}$ N), North-East (NE)  
591 ( $32.5^{\circ}$ N- $40^{\circ}$ N) in longitude band  $70^{\circ}$ E- $120^{\circ}$ E, South-West (SW) ( $22.5^{\circ}$ N- $32.5^{\circ}$ N), and  
592 North-West (NW) ( $32.5^{\circ}$ N- $40^{\circ}$ N) at  $20^{\circ}$ E- $70^{\circ}$ E longitude range.



593

594 Figure 5. Time series of anomalies in zonal wind estimated for (a) North-West, (b) South-  
595 West, (c) North-East and (d) South-East sectors of ASMA. The trend analysis was  
596 performed at 95% confidence interval by using robust regression analysis. (e) The strength  
597 of the anticyclone was estimated from the zonal wind difference between (30°N-40°N)-  
598 (10°N-20°N) in the longitude band of 50°E-90°E.

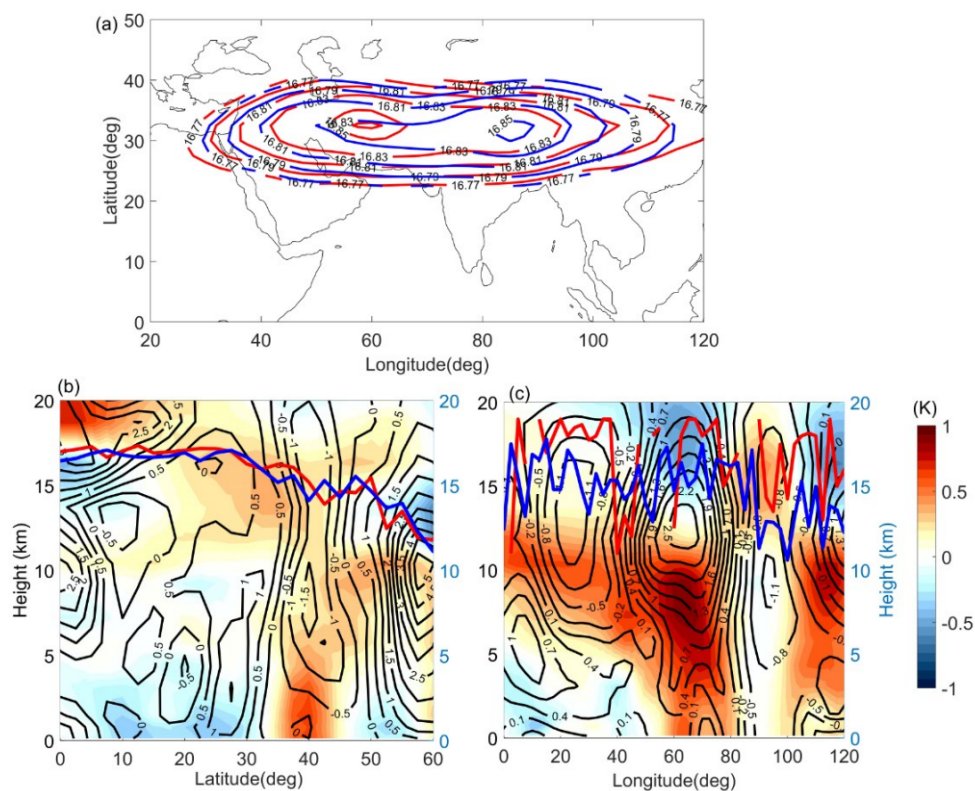


599

600 Figure 6. (a) ASMA variability during active and break phases of Indian monsoon obtained  
601 from GPH at 100 hPa. Red line indicates the active and blue line for break phase of Indian  
602 monsoon. (b) Latitude-altitude cross-section of temperature (colour shaded, K) and zonal  
603 wind anomalies (contour lines, m/s) which are estimated from difference between active  
604 and break phases of Indian Monsoon in the longitude band of 80°E-90°E. (c) Longitude-  
605 altitude cross-section of temperature and wind anomalies averaged between 30°N-40°N.  
606 The red and blue lines in Figure 6b & 6c denotes the tropopause altitude during active and  
607 break spells of Indian monsoon estimated using GNSS RO data.

608

609



610

611

612 Figure 7. (a) ASMA variability obtained from GPH at 100hPa during strong and weak

613 monsoon years calculated based on high resolution rainfall data in band of 5°N-30°N,

614 70°N-95°E grid. Red line indicates the strong and blue line for weak monsoon years. (b)

615 Latitude-altitude cross-section of temperature (colour shaded, K) and zonal wind

616 anomalies (contour lines, m/s) which are estimated from difference between strong and

617 weak monsoon years in the longitude band of 80°E-90°E. (c) Longitude-altitude cross-

618 section of temperature and wind anomalies averaged between 30°N-40°N. Red and blue

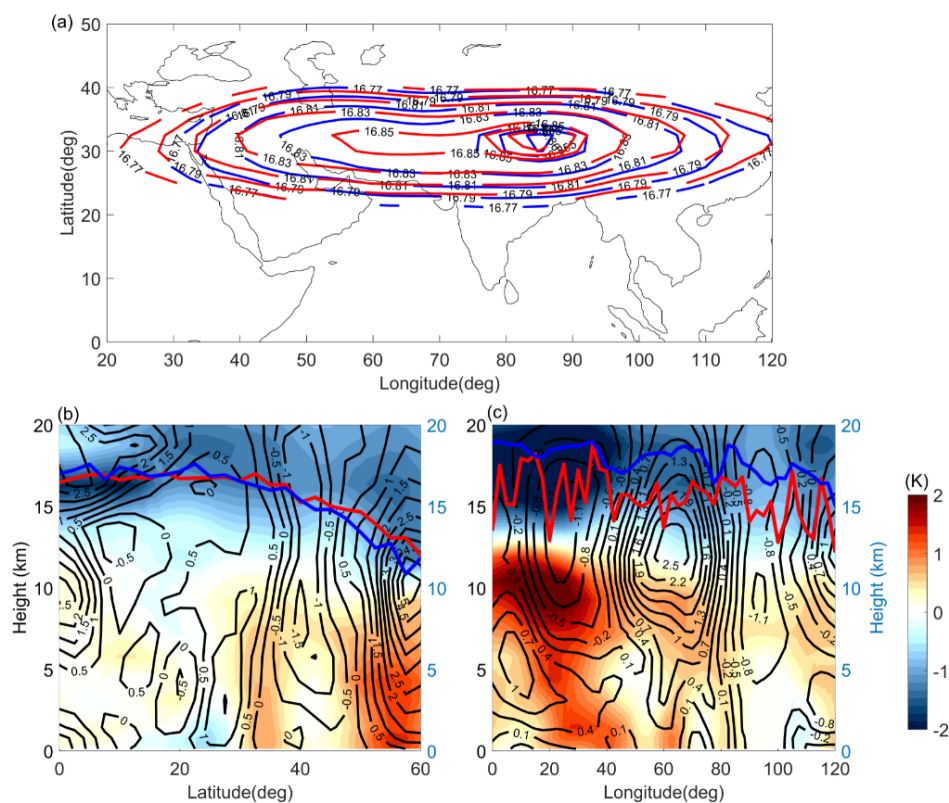
619 lines in Figure 7b & 7c denote the tropopause altitude during strong and weak monsoon

620 years estimated using GNSS RO data.

621



622



623

624 Figure 8. (a) ASMA variability obtained from GPH at 100 hPa during strong La Niño and El  
625 Niño years. Red and blue lines indicate the La Niño and El Niño years. (b) Latitude-  
626 altitude cross-section of temperature (colour shaded, K) and zonal wind anomalies  
627 (contour lines, m/s) which are estimated from difference between La Niño and El Niño  
628 years in the longitude band of 80°E-90°E. (c) Longitude-altitude cross-section of  
629 temperature and zonal wind anomalies averaged between 30°N-40°N. The red and blue  
630 lines in Figure 8b & 8c denote the tropopause altitude during La Niño and El Niño years  
631 estimated from GNSS RO data.

632

633